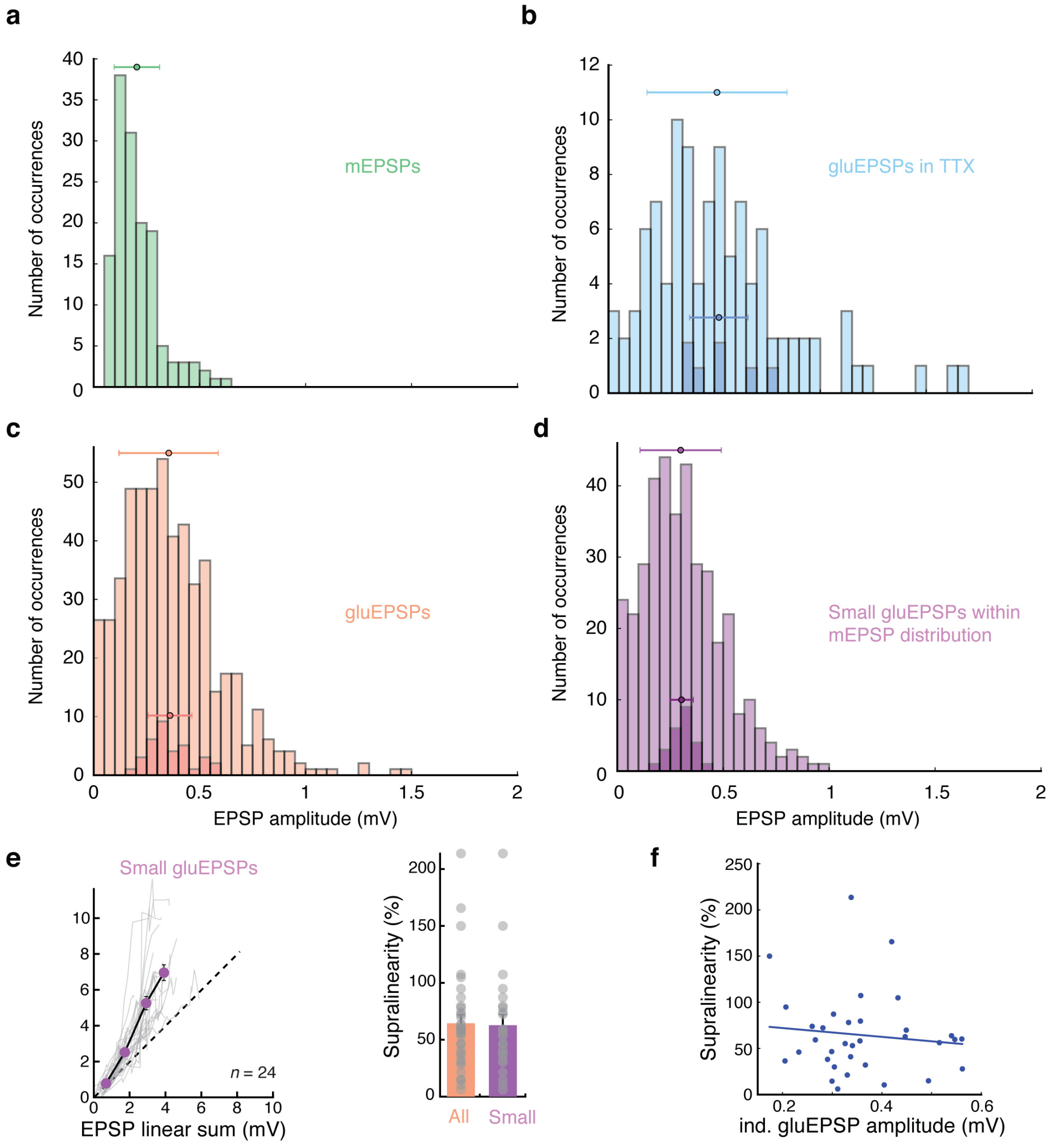

**Supplementary Figure 1**

2-photon glutamate uncaging evokes EPSPs with physiological amplitudes in MECII stellate cells.

(**a**) Distribution of peak amplitudes of miniature EPSPs (mEPSPs) recorded in the presence of TTX.

(**b**) Distribution of individual peak amplitudes of EPSPs evoked by uncaging (gluEPSPs) on single spines in the presence of TTX.

(**c**) Distribution of individual peak amplitudes of EPSPs evoked by uncaging on single spines.

(**d**) Subpopulation of recordings from **c** with peak EPSP amplitudes within mean ± 2SD (0.2 ± 0.2 mV) of the mEPSP peak amplitude distribution (”small gluEPSPs”).

In **b**–**d**, darker bars represent distribution of average EPSP peak amplitudes across all spines for each recording.

(**e**) Supralinearity for all gluEPSPs and for a subset of “small gluEPSPs” (see **d**) is similar: 64 ± 8% ($n = 34$) and 63 ± 9% ($n = 24$) for all gluEPSPs and “small gluEPSPs”, respectively (Mann-Whitney $U$ test: $P = 0.77$).

(**f**) Supralinearity of recordings did not depend on the individual spine gluEPSP amplitude (Linear regression: $r = –0.11$, $P = 0.52$, $n = 34$).

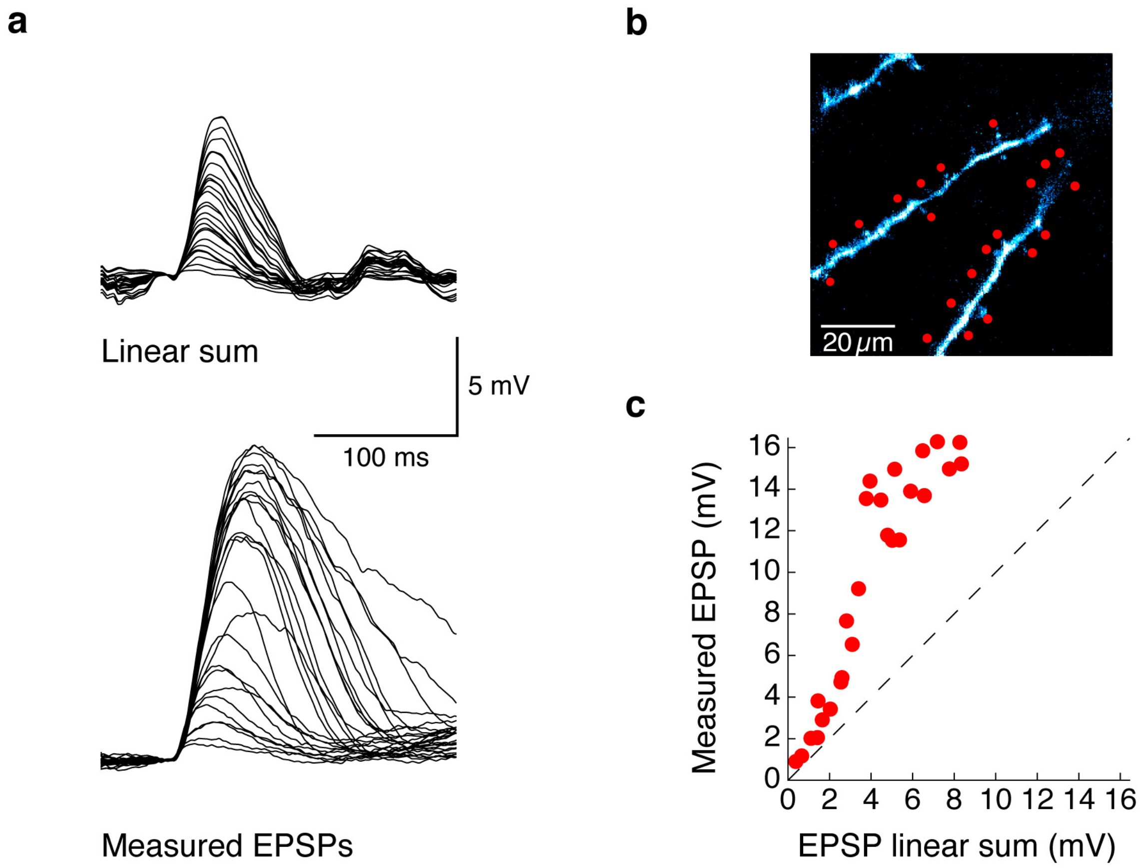

**Supplementary Figure 2**

Supralinear integration evoked by uncaging on two dendrites in a in MECII stellate cell.

(**a**) Somatic voltage responses to increasing number of stimulated synapses on two neighbouring dendrites (indicated in **b**; uncaging interval: 0.6 ms). Top traces show arithmetic sum expected from the individual responses, bottom traces show experimentally recorded responses.

(**b**) Two-photon image of two MECII stellate cell dendrites filled with Alexa594. Uncaging locations are indicated by red circles.

(**c**) When activating inputs on two dendrites, amplitudes of somatically recorded gluEPSPs were markedly larger than the arithmetic sum of the individual responses (dashed line indicates unity).

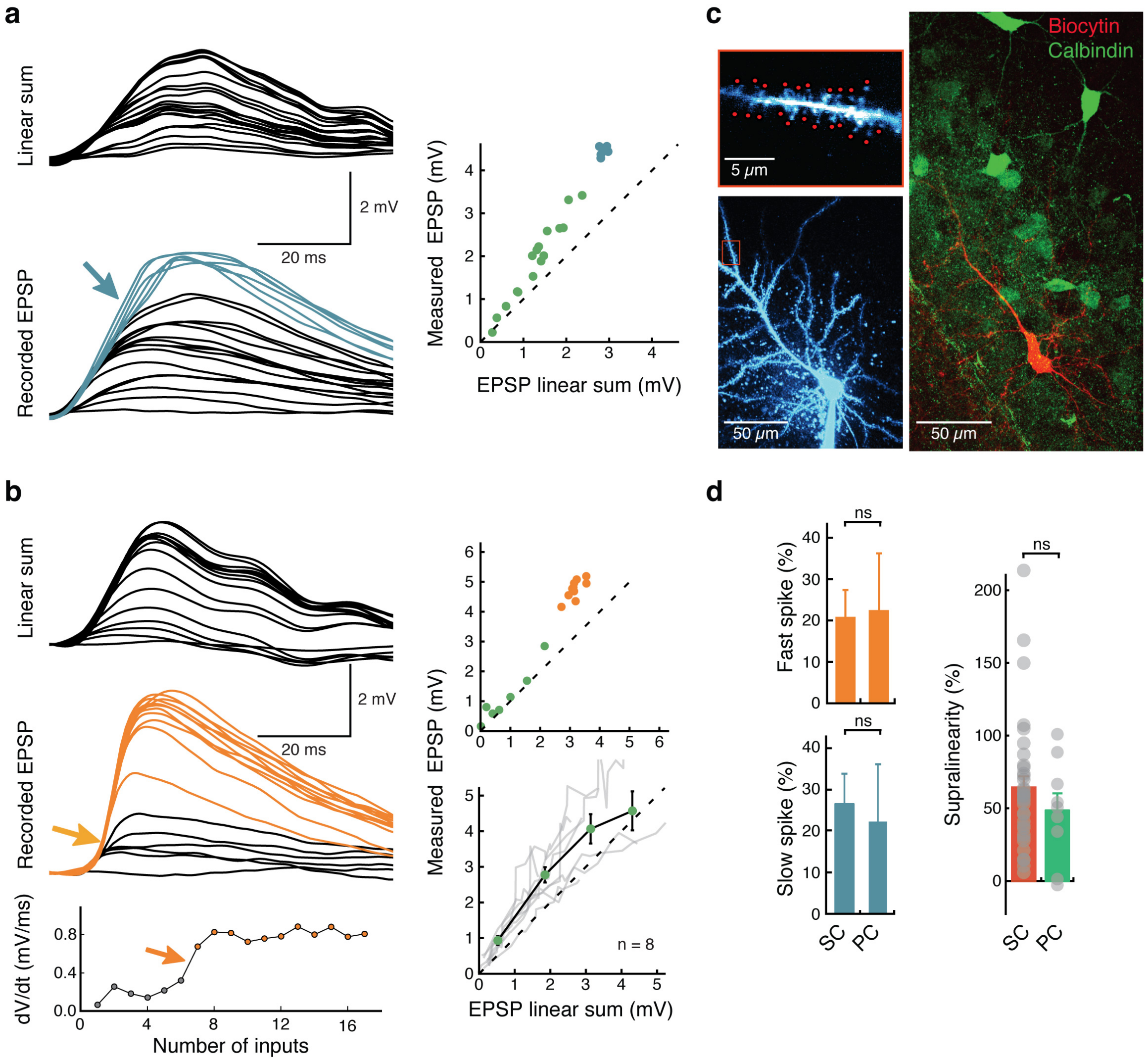

**Supplementary Figure 3**

Supralinear dendritic integration and dendritic spikes in MECII pyramidal cells.

(**a**,**b**) Somatic voltage responses to uncaging on an increasing number of spines in a MECII pyramidal cell.

(**a**) (Left panels) Top traces show arithmetic sum expected from the individual responses, bottom traces show recorded responses (22 spines, 0.6 ms uncaging interval). Blue traces indicate the presence of a slow dendritic spike (see Methods). (Right panel) The amplitudes of somatically recorded gluEPSPs were markedly larger than the arithmetic sum of the individual responses (dashed line indicates unity).

(**b**) (Left panels) Some recordings exhibit fast dendritic spikes (orange traces and orange arrow), detected by a step-like increase in the maximal rate of rise (bottom; see Methods). (Right panels) Top: single experiment; bottom: summary of 8 experiments. Grey lines represent individual experiments, the black line connects binned averages across experiments (green).

(**c**) Left bottom, MECII pyramidal cell filled with Alexa 594 dye (same cell as in **a**). Left top, selected dendrite with uncaging spots (red) at higher magnification. Right, the biocytin-filled cell (red) was located within a cluster of Calbindin+ cells (green).

(**d**) MECII stellate cells (SC) and pyramidal cells (PC) integrate dendritic inputs in a similar manner with comparable occurrences of fast (21 ± 7% and 22 ± 14% for SC and PC, respectively, Fisher's exact test: *P* = 1) and slow dendritic spikes (26 ± 7% and 22 ± 14% for SC and PC, respectively, Fisher's exact test: *P* = 1) and comparable degrees of supralinearity (64 ± 8%, *n* = 34 for SC and 49 ± 12%, *n* = 9 for PC, Mann-Whitney *U* test: *P* = 0.42).

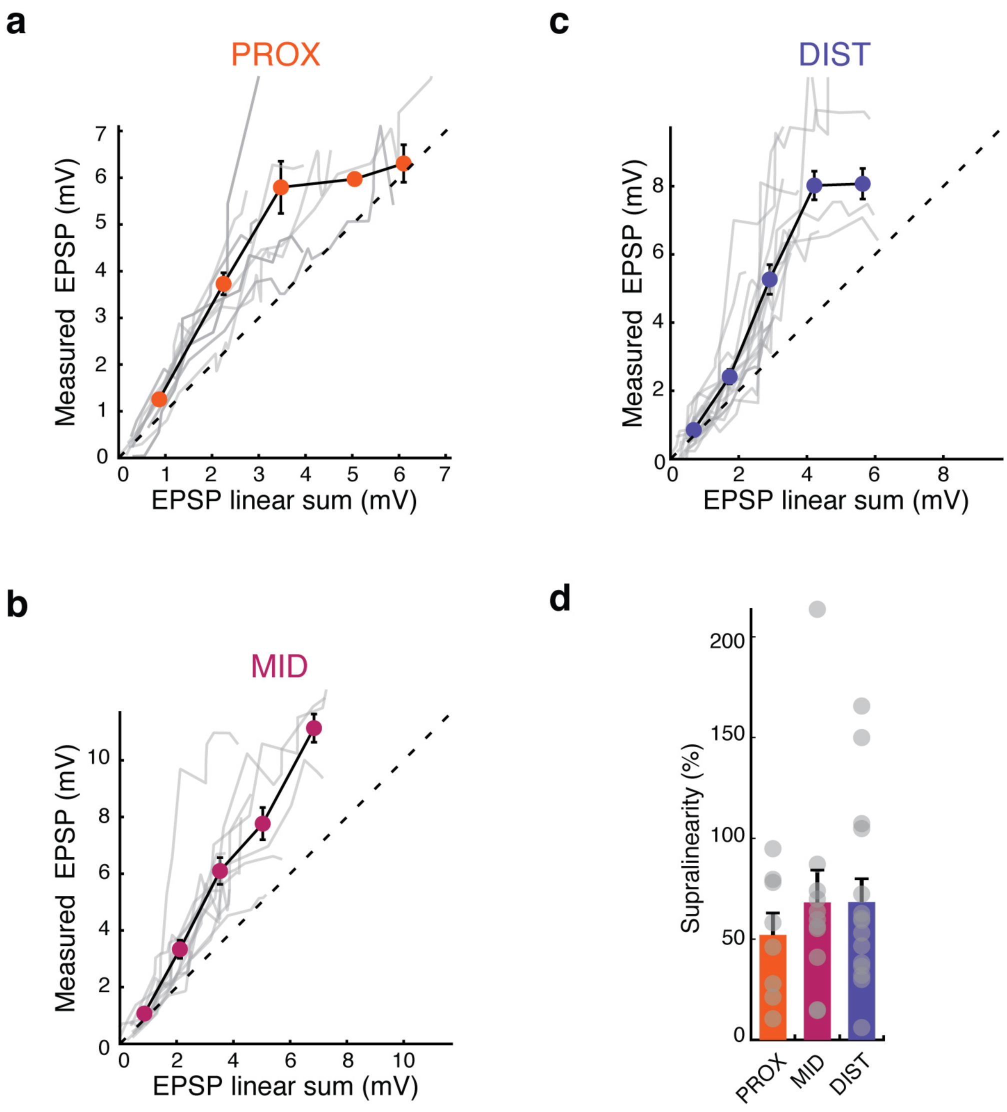

**Supplementary Figure 4**

The degree of supralinear dendritic integration is independent of uncaging location in MECII stellate cells.

(**a**–**c**) The amplitudes of somatically recorded gluEPSPs were plotted against the amplitudes of the arithmetic sums of the individual responses (dotted line indicates unity). Grey lines represent individual experiments, the black line connects binned averages across experiments (colored dots).

(**a**) Uncaging on proximal dendrites (<60 µm distance from soma).

(**b**) Uncaging on middle dendrites (60–120 µm distance from soma).

(**c**) Uncaging on distal dendrites (>120 µm distance from soma).

(**d**) No significant differences in the degree of supralinearity were observed between proximal (52 ± 11%, *n* = 8), middle (68 ± 16%, *n* = 11) and distal (68 ± 12%, *n* = 15) uncaging locations (one-way ANOVA: *P* = 0.68, *F* = 0.39).

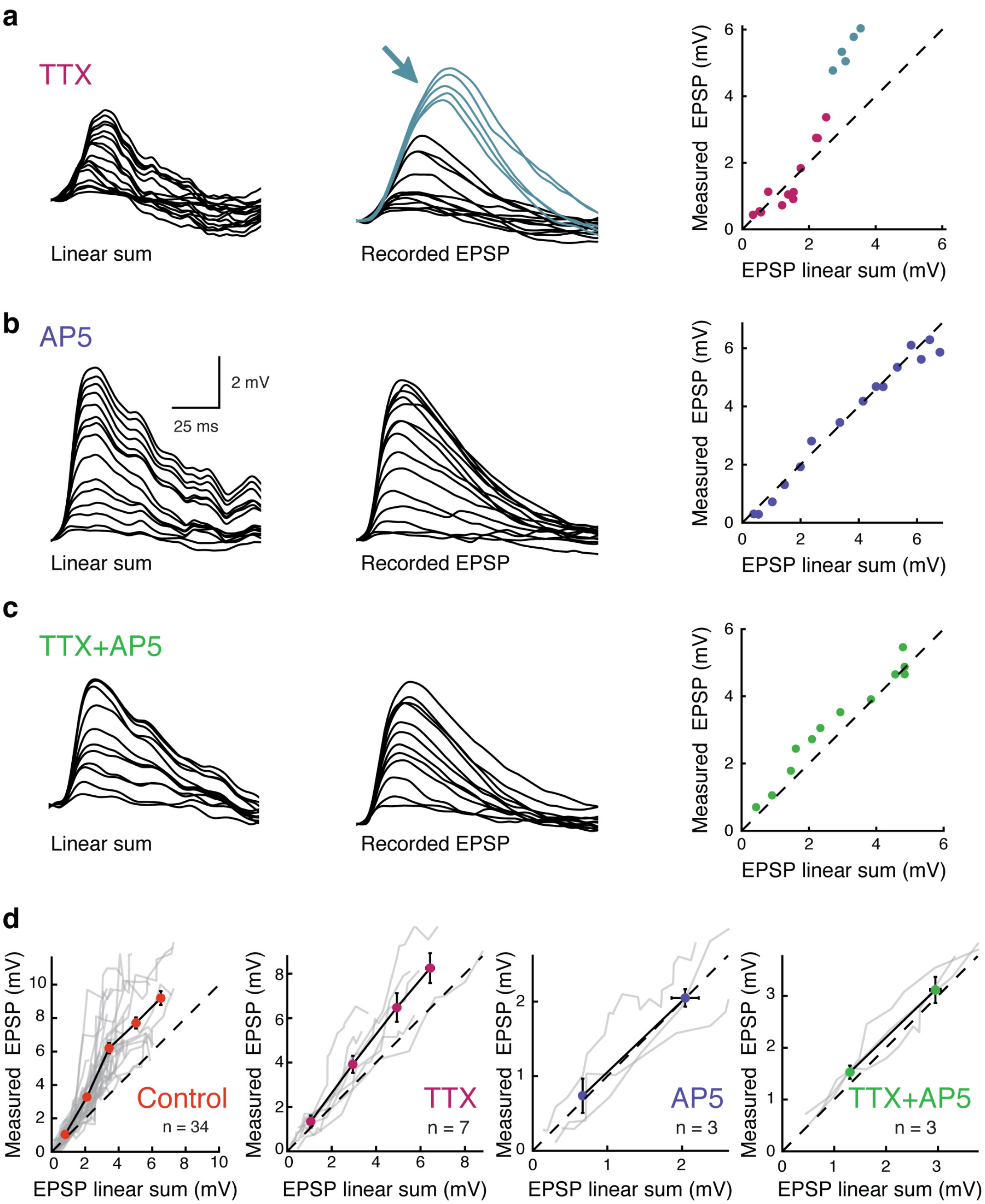

**Supplementary Figure 5**

Supralinear integration depends on voltage-gated sodium (Nav) channels and NMDA receptors (NMDARs).

(**a**–**c**) Some recordings from MECII stellate cells still exhibit supralinear summation and slow dendritic spikes when Nav channels are blocked with TTX (**a**). Supralinearity is significantly reduced and dendritic spikes are abolished by blocking NMDARs with AP5 (**b**), or NMDARs and Nav channels with AP5 and TTX (**c**).

(**d**) Summary of the recordings in TTX (left), AP5 (middle) and TTX and AP5 (right). Grey lines show individual experiments, black line connects binned averages across experiments.

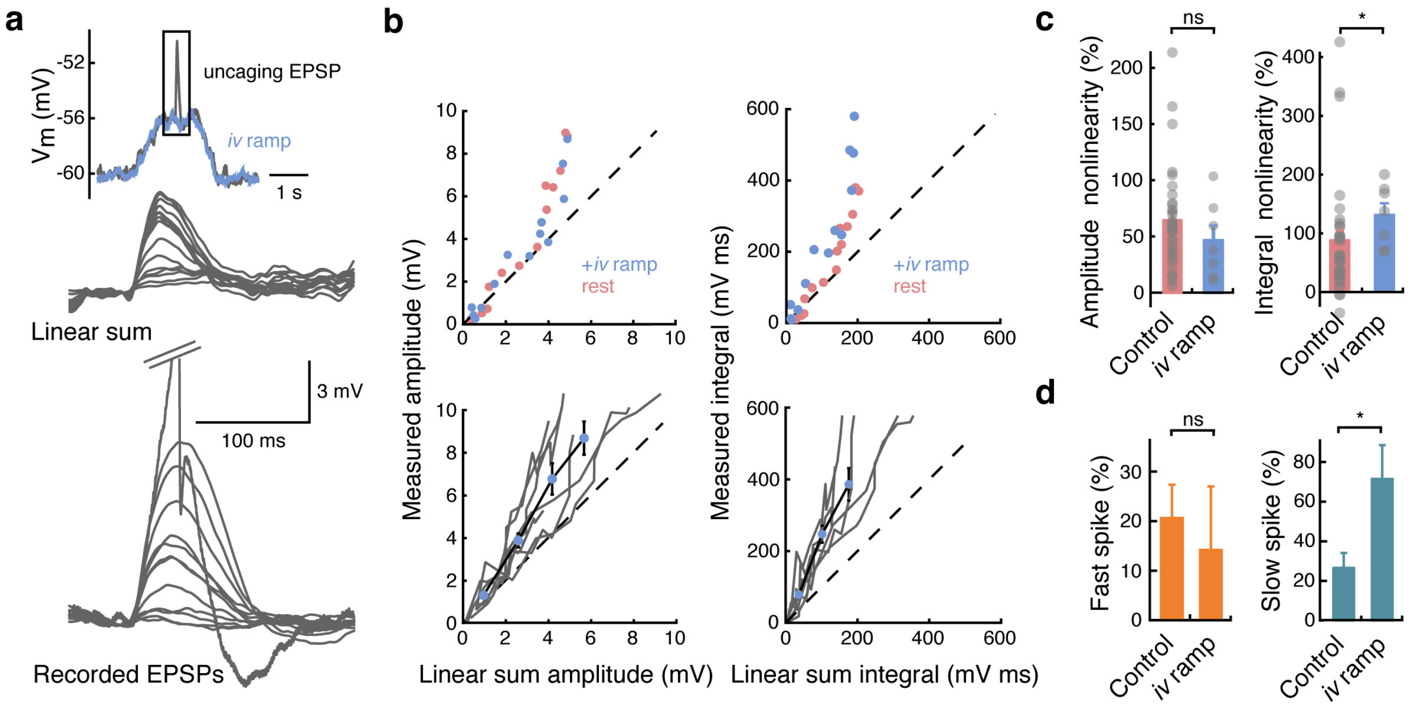

**Supplementary Figure 6**

Dendritic integration during *in vivo*-like membrane potential dynamics in MECII stellate cells.

(**a**) Top: Somatic voltage responses to uncaging on an increasing number of spines (grey) during *in vivo*-like membrane potential dynamics (blue), mimicking a slow depolarisation observed in MECII neurons during firing field crossings *in vivo* (Schmidt-Hieber & Häusser, 2013). Middle traces show arithmetic sum expected from the individual responses, bottom traces show recorded responses (13 spines, 1.0 ms stimulation interval).

(**b**) The amplitudes and integrals of somatically recorded gluEPSPs were markedly larger than the arithmetic sum of the individual responses (dashed line indicates unity). Top: single experiment with (blue) or without (pink) *in vivo*-like membrane potential dynamics. Bottom: summary of 7 experiments with *in vivo*-like membrane potential dynamics. Grey lines represent individual experiments, the black line connects binned averages across experiments (blue).

(**c**) EPSP integrals (Mann-Whitney *U* test: $P = 0.01$) but not amplitudes (Mann-Whitney *U* test: $P = 0.62$), show increased supralinearity during *in vivo*-like membrane potential dynamics ($n = 7$) vs control ($n = 34$).

(**d**) Slow (Fisher's exact test $P = 0.01$) but not fast (Fisher's exact test $P = 0.94$) dendritic spikes occur more frequently during *in vivo*-like membrane potential dynamics ($n = 7$) vs control ($n = 34$).

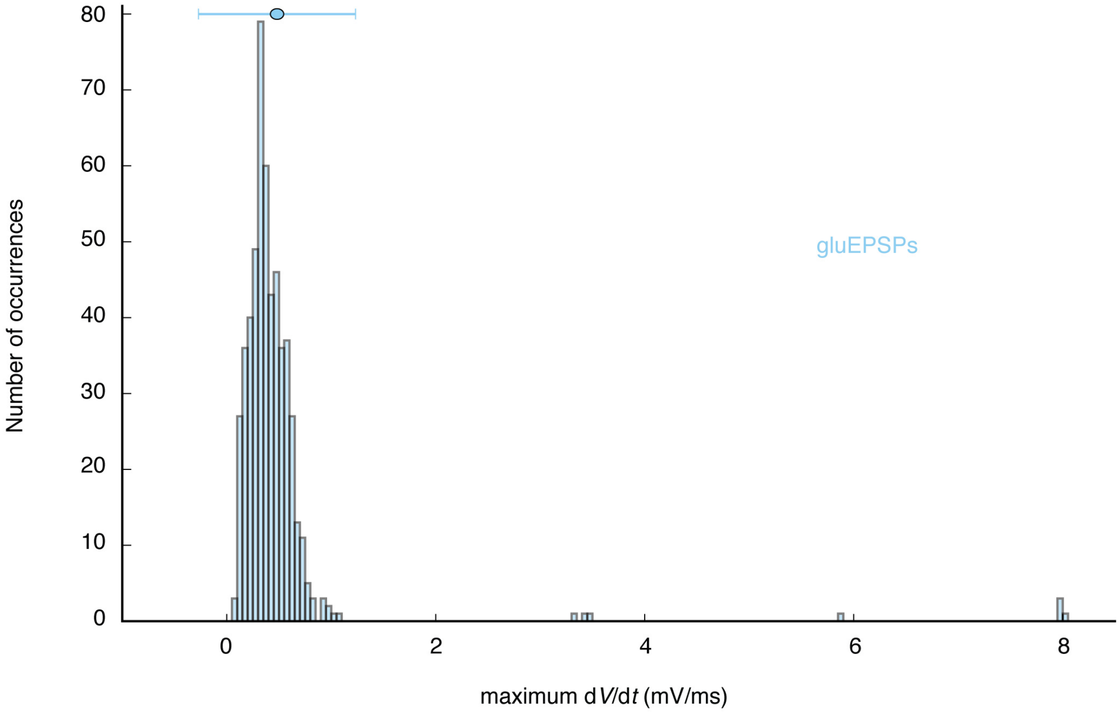

**Supplementary Figure 7**

Distribution of maximum rates of rise of gluEPSPs.

The histogram shows the distribution of maximum d*V*/d*t* values of gluEPSPs evoked by uncaging on individual and multiple spines (≤1 ms stimulation interval) in MECII stellate cells *in vitro*. The largest d*V*/d*t* values were associated with events exhibiting dendritic spikes.

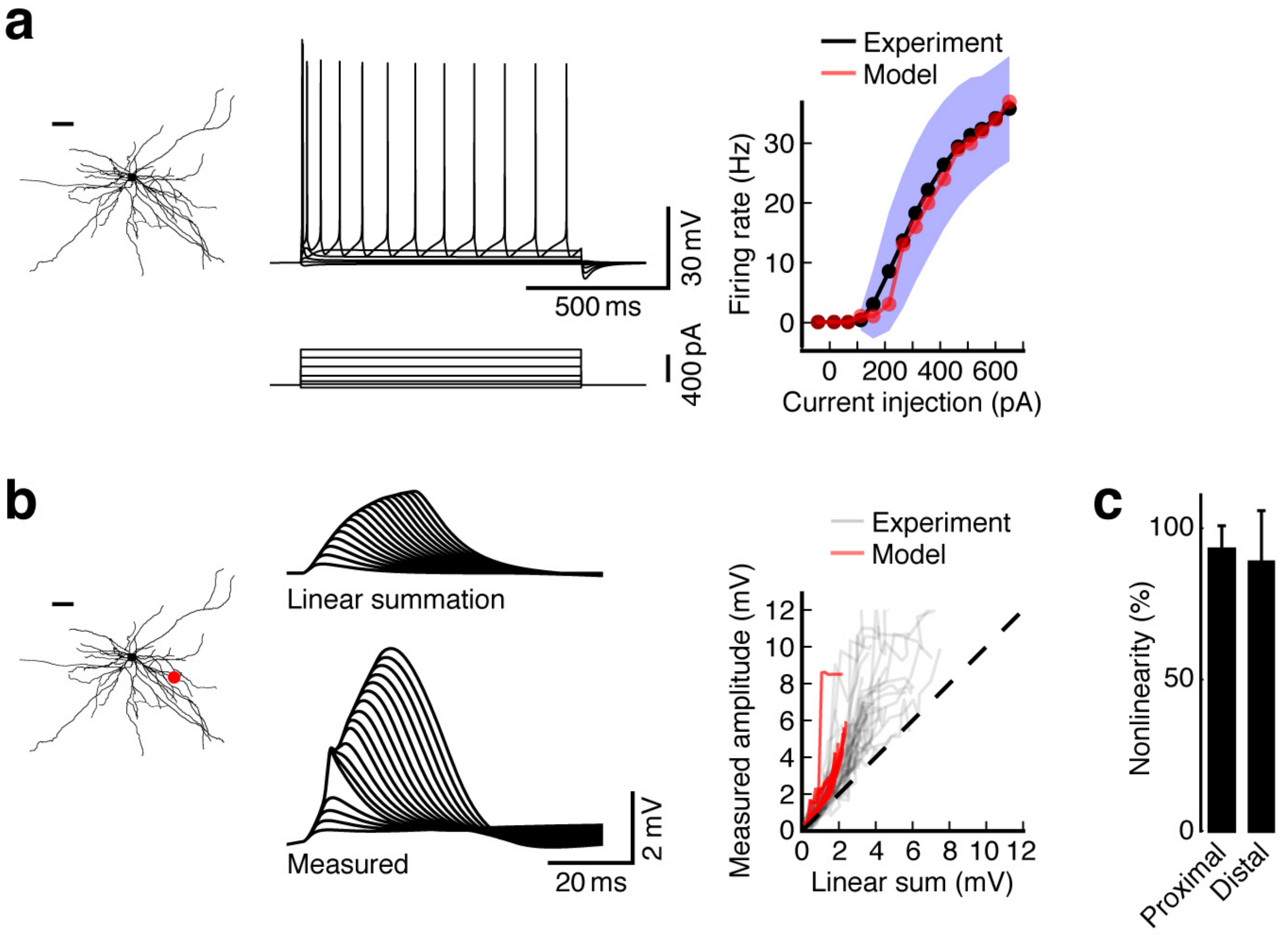

**Supplementary Figure 8**

Calibration of a detailed active compartmental MECII stellate cell model.

(**a**) A detailed compartmental model was developed to faithfully reproduce experimentally determined *f-I* relationships. (Left) Morphological reconstruction of an MECII stellate neuron (Garden *et al*., 2008; scale bar: 50 µm). (Middle) Model $V_\mathrm{m}$ responses to sustained current injections. (Right) Firing frequency was plotted against sustained current injection amplitudes for experimental (black) and model (red) data. The grey shaded area indicates the region between mean – S.D. and mean + S.D. of the experimental data.

(**b**) The compartmental model captures experimentally determined input-output relationships of single dendritic branches. (Left) Morphological reconstruction with the location of synaptic conductance change indicated (red; scale bar: 50 µm). (Middle) Top traces show the arithmetic sum of model responses to stimulation of individual synapses on single dendritic branches. Bottom traces show the model responses to activating an increasing number of synapses on a single branch at an interval of 1 ms. Responses are consistent with experimental observations (see e.g. Fig. 2a, top). (Right) Input-output curves of individual dendritic branches of the same model cell (red) capture the variety of responses found across the experimental data set (grey).

(**c**) The summary bar graph shows nonlinearity across proximal (100 µm distance from soma; 93 ± 8% nonlinearity; *n* = 13 dendrites) and distal dendritic branches (175 µm distance from soma; 89 ± 17% nonlinearity; *n* = 18 dendrites) of the compartmental model.

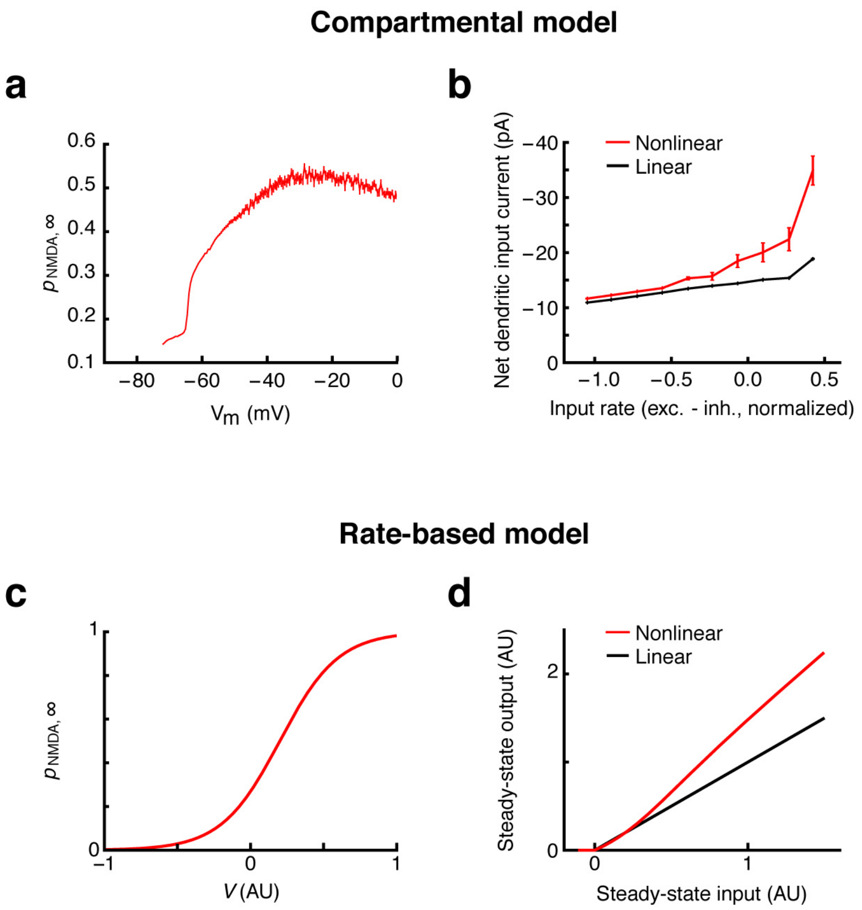

**Supplementary Figure 9**

Dendritic nonlinearities are robustly engaged during grid cell firing.

(**a**,**b**) Grid cell firing simulations were performed in a compartmental model of an MECII stellate cell (same simulation parameters as shown in Figs. 3 and 6). A linear compartmental model was generated by fixing the open probabilities of Nav channels and NMDARs at $V = –60$ mV.

(**a**) NMDAR steady-state open probability ($p_{\mathrm{NMDA},\infty}$) was plotted against somatic membrane potential during grid cell firing. Note that $p_{\mathrm{NMDA},\infty}$ sigmoidally depends on somatic membrane potential; and that NMDARs are driven into their highly nonlinear range during grid firing field crossings (cf. Schmidt-Hieber and Häusser, 2013; and Domnisoru et al. 2013).

(**b**) Net dendritic input current (sum of all ionic and synaptic currents) is plotted against normalized synaptic input rate (computed as the difference between excitatory and inhibitory input rates). There is a strong dendritic drive resulting from nonlinear dendritic conductances - NMDA currents and sodium currents - justifying the nonlinear input-output relationship used in the rate-based model (**c** and **d**).

(**c**,**d**) NMDAR implementation in our rate-based model.

(**c**) NMDAR steady-state open probability was plotted against membrane potential (eqn. 9, see Online Methods). Same plot as in Fig. 5b, left panel. Sigmoidal dependence on membrane potential is compatible with predictions from the compartmental model (**a**).

(**d**) Steady-state output rate was plotted against steady-state input rate in the presence (red) or in the absence (black) of NMDARs (eqns. 3, 8, and 9, see Online Methods). Same plot as in Fig. 5b, right panel. Implementing NMDARs as a multiplicative term (eqn. 3) captures their contribution to the input-output transformation in MECII principal neurons.

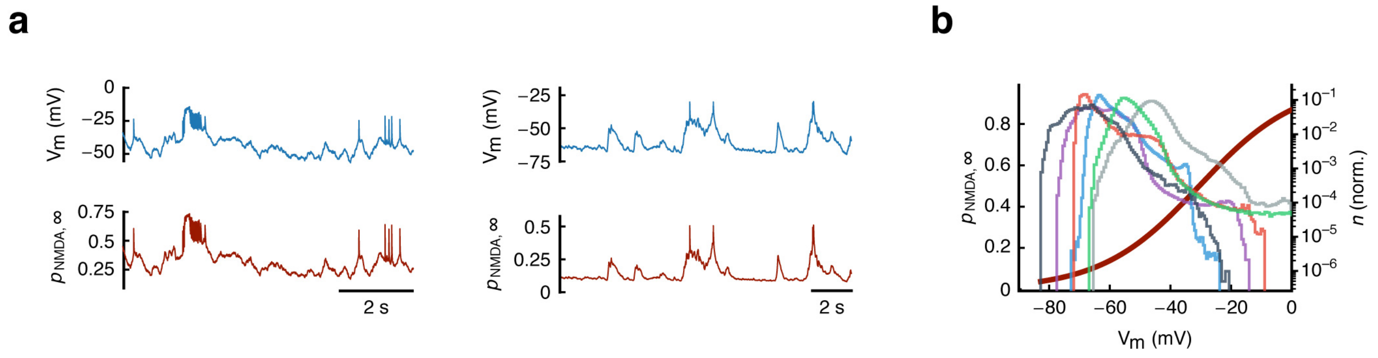

**Supplementary Figure 10**

Nonlinear recruitment of NMDARs during dendritic *in vivo* membrane potential dynamics.

(**a**,**b**) Membrane potential trajectories from $n = 6$ putative dendritic *in vivo* recordings (see also Fig. 4 and Supplementary Fig. 12) were used to compute the steady-state open probability of the NMDAR channel from our MECII stellate cell compartmental model.

(**a**) Two representative *in vivo* dendritic membrane potential recordings (top) and the corresponding computed NMDAR steady-state open probabilities (bottom). Note that NMDAR conductances are already engaged in the subthreshold regime, and are nonlinearly enhanced during dendritic spikes and plateau potentials.

(**b**) The red sigmoid curve shows a plot of NMDAR steady-state open probability (left y axis) against membrane potential. The histograms show membrane potential distributions for $n = 6$ *in vivo* recordings from putative dendrites (logarithmic y axis on the right; histograms were normalized to yield an integral of 1). The distributions of dendritic membrane potential span a wide range of the NMDAR open probability curve, and demonstrate that NMDARs at active synapses are driven robustly into their nonlinear range during *in vivo* dendritic membrane potential trajectories.

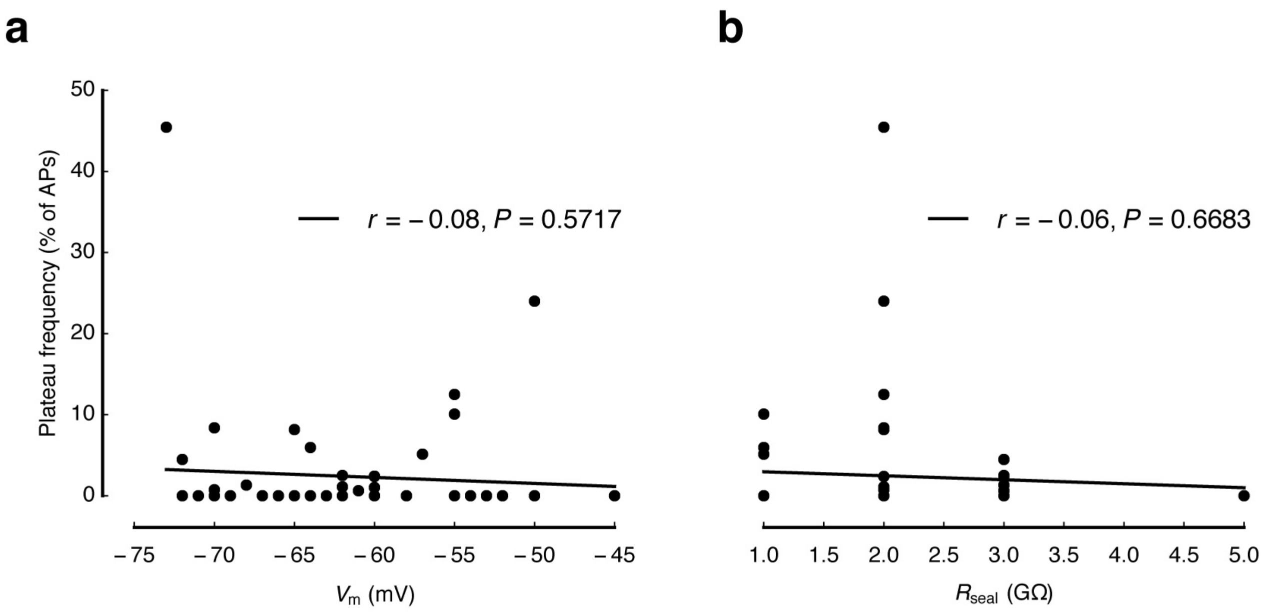

**Supplementary Figure 11**

Plateau potentials do not depend on recording parameters during *in vivo* recordings from MECII stellate cells.

(**a**) No significant correlation between plateau potential frequency and *in vivo* resting membrane potential.

(**b**) No significant correlation between plateau potential frequency and seal resistance. Straight black lines represent linear regressions ($n$ = 58 recordings).

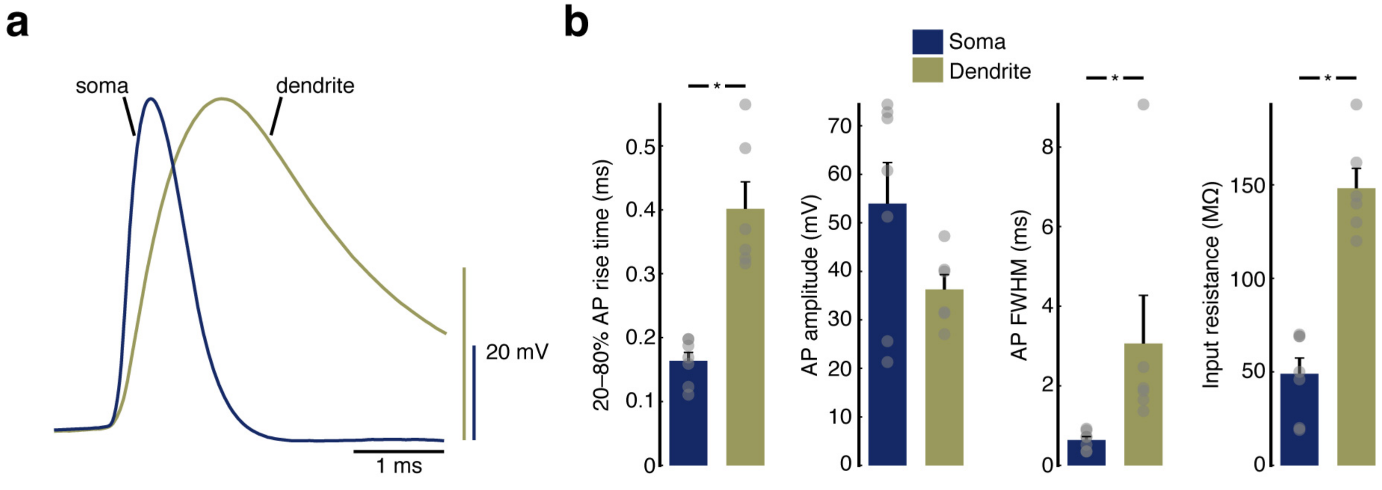

**Supplementary Figure 12**

Electrophysiological parameters of putative somatic and putative dendritic *in vivo* recordings from MECII stellate cells.

(**a**) Example action potential waveforms from putative somatic (blue) and putative dendritic (green) *in vivo* recordings, normalized to the same peak amplitude. Note the slower risetime, larger half duration and smaller amplitude of the action potential in the dendritic recording.

(**b**) Comparison of 20–80% AP rise time (soma: 0.16 ± 0.01 ms, $n = 7$ recordings; dendrite: 0.40 ± 0.04 ms, $n = 6$; $P < 0.005$), AP amplitude (from threshold; soma: 54 ± 8 mV, $n = 7$; dendrite: 36 ± 3 mV, $n = 6$; $P = 0.11$), AP full width at half-maximal amplitude (FWHM; soma: 0.64 ± 0.09 ms, $n = 7$; dendrite: 3.06 ± 1.21 ms, $n = 6$; $P < 0.005$), and input resistance (soma: 49 ± 8 MΩ, $n = 7$; dendrite: 148 ± 11 MΩ, $n = 6$; $P < 0.005$).

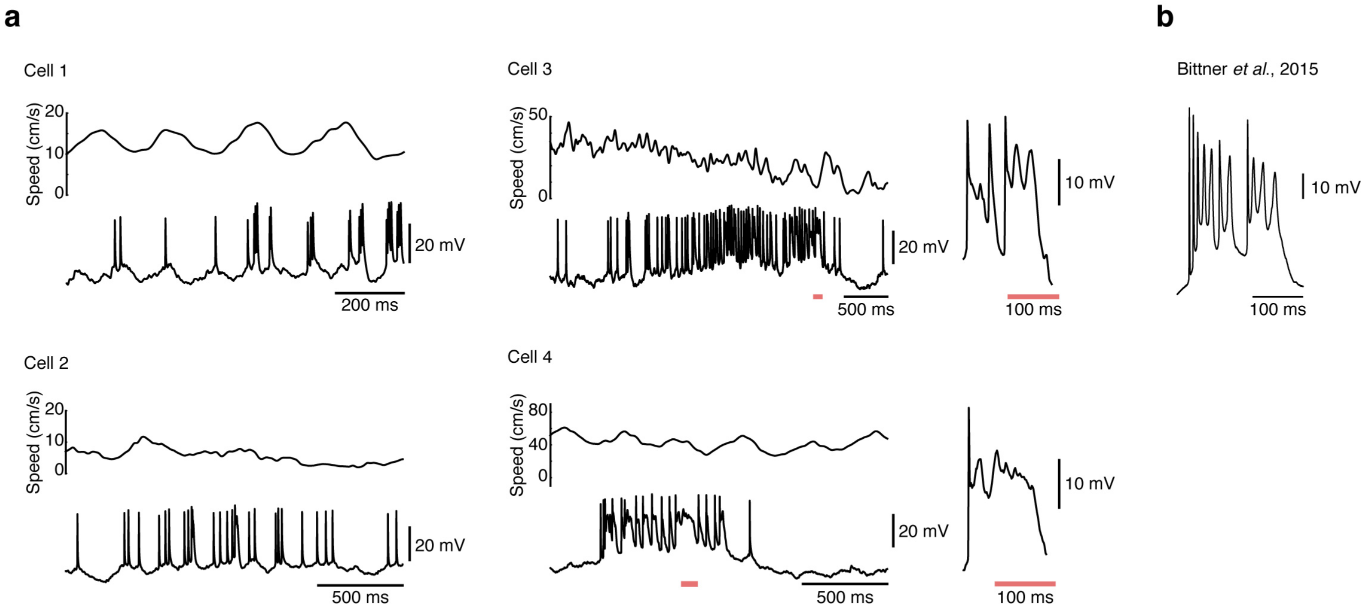

**Supplementary Figure 13**

Plateau potentials during navigation in virtual reality.

(**a**) Traces show example *in vivo* recordings from 4 MECII neurons that produced plateau potentials during running. For cells 3 and 4, examples of plateau potentials are shown at an enlarged scale in the right panels (indicated by the corresponding red horizontal scale bars at the bottom of the left panels).

(**b**) Example plateau potentials from another publication are shown for comparison (adapted with permission from Fig. 1g in Bittner *et al*., 2015).

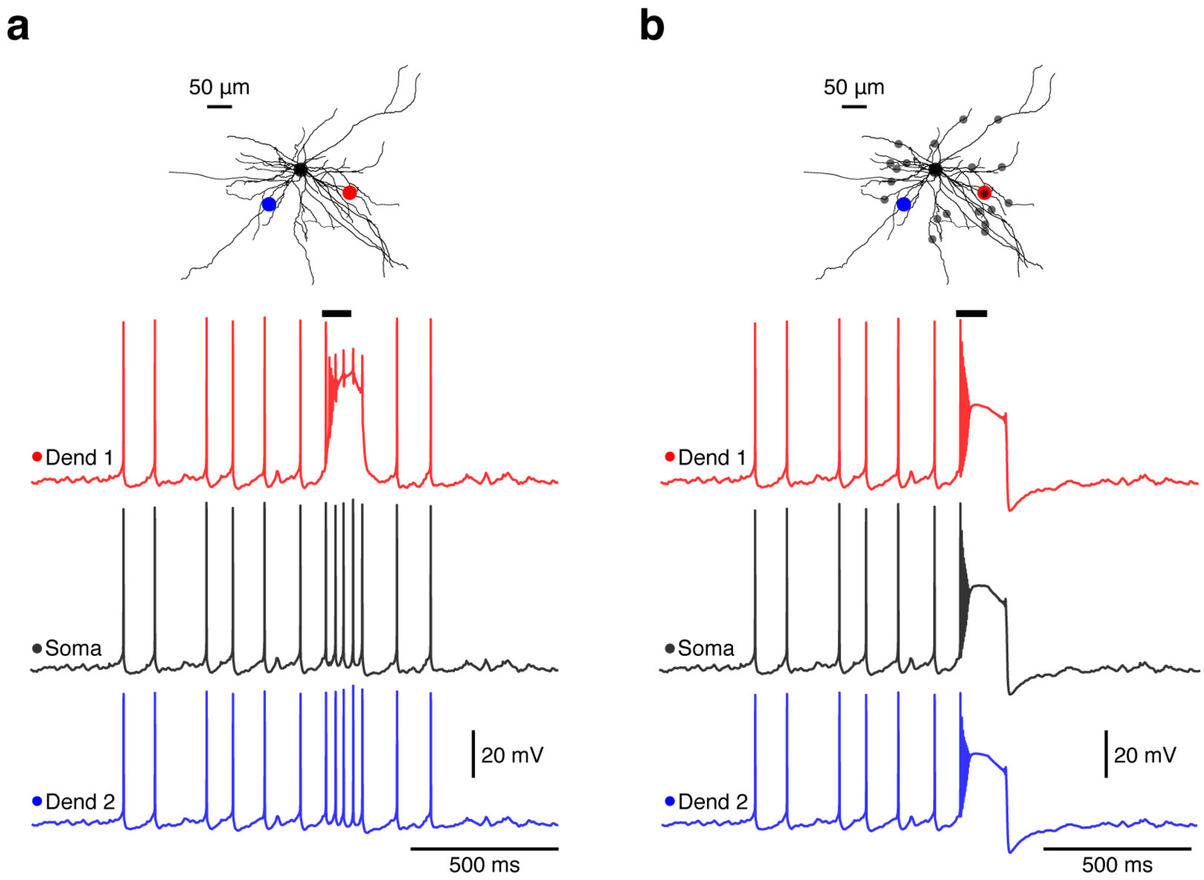

**Supplementary Figure 14**

Plateau potentials are spatially confined to their dendritic site of origin.

(**a**,**b**) On top of the synaptic conductance changes used for simulating grid cell firing as shown in Fig. 3 and 6, additional synaptic conductance changes were activated during 100 ms at 100 Hz (black bars above traces) to evoke plateau potentials.

(**a**) Plateau potential evoked by activation of a single synaptic conductance change in a single dendritic branch (red). Membrane potential at the soma (black) and in a different dendritic branch (blue) shows an increase in firing rate, but no discernible plateau potential.

(**b**) Same simulation as in **a**, but with multiple synaptic conductance changes distributed across the dendritic tree (grey filled circles). To produce a noticeable plateau potential at the soma, synaptic inputs (each with the same conductance amplitude as in **a**) had to be distributed across at least 20 separate dendritic branches and simultaneously activated. Thus, only maximally strong (and likely rare) synchronous synaptic input regimes can produce plateau potentials that succeed to propagate to the soma.

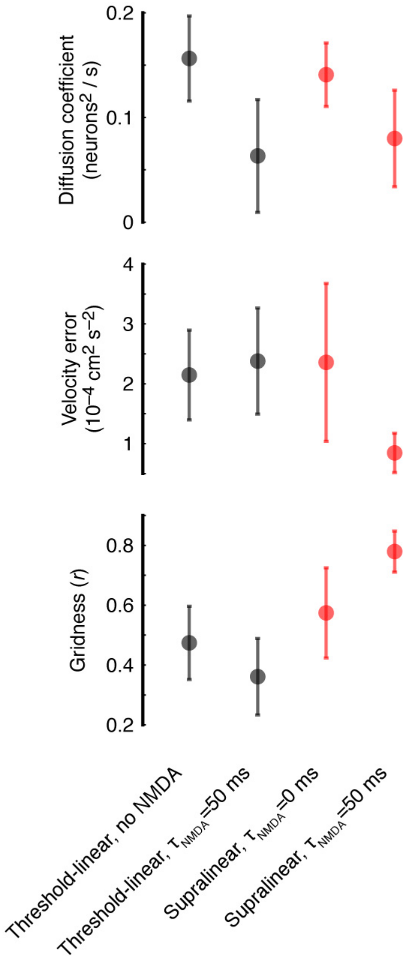

**Supplementary Figure 15**

Supralinearity and slow time constant improve robustness of the rate code.

From top to bottom: network diffusion coefficient in the absence of velocity inputs, summed squared velocity error, and gridness for CAN network simulations under the following conditions (see Online Methods for equations):

(1) threshold-linear integration in the absence of NMDARs
$k_V$ = 0.88 in eqn. 2, $k_{NMDA}$ = 0 in eqn. 3

(2) threshold-linear integration with slow NMDARs
$k_V$ = 0.4 in eqn. 2, $k_{NMDA}$ = 0.16 in eqn. 3, $\tau_{NMDA}$ = 50 ms in eqn. 8, $p_\infty(V) = 1$ replaces eqn. 9
parameters were chosen to keep mean firing rates as well as the ratio $k_{NMDA} / k_V$ approximately constant across simulations

(3) supralinear integration with instantaneous NMDARs
$k_V$ = 0.88 in eqn. 2, $k_{NMDA}$ = 0.4 in eqn. 3, $\tau_{NMDA}$ = 0 ms in eqn. 8

(4) supralinear integration with slow NMDARs
$k_V$ = 0.88 in eqn. 2, $k_{NMDA}$ = 0.4 in eqn. 3, $\tau_{NMDA}$ = 50 ms in eqn. 8

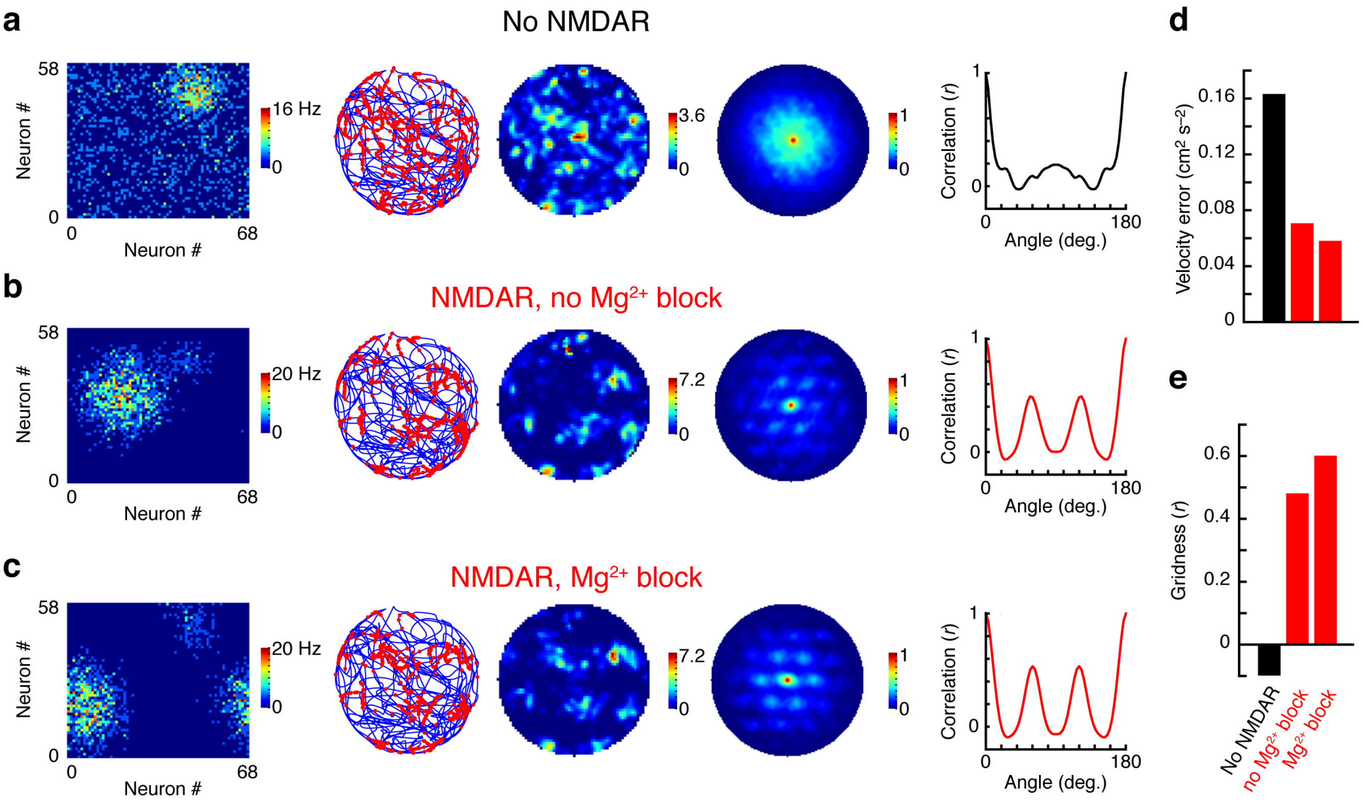

**Supplementary Figure 16**

NMDARs promote stable attractor states in a spiking CAN model of grid cell firing.

(**a**–**c**) We modified a previously published spiking CAN model of grid cell firing (Pastoll *et al*., 2013). Theta-modulated and static feedforward excitatory currents in the original model were replaced by Poisson spike trains driving synaptic conductance changes containing either only AMPAR (**a**), or a combination of AMPAR and NMDAR without voltage dependence (**b**) or with voltage-dependence (**c**). Conductances were adjusted to yield similar mean network firing rates. The color-coded maps (left) show the firing rates in a network of 58 x 68 excitatory integrate-and-fire neurons. Circular maps show (from left to right) animal trajectory (blue) and spikes (red circles), color-coded spatial firing rate map, and autocorrelation matrix of the spatial firing rate map. Right panels: Correlation between rotated autocorrelation maps plotted against the rotation angle.

(**d**,**e**) Comparison of summed squared velocity error (**d**) and gridness (**e**) for the 3 models from **a**–**c**.

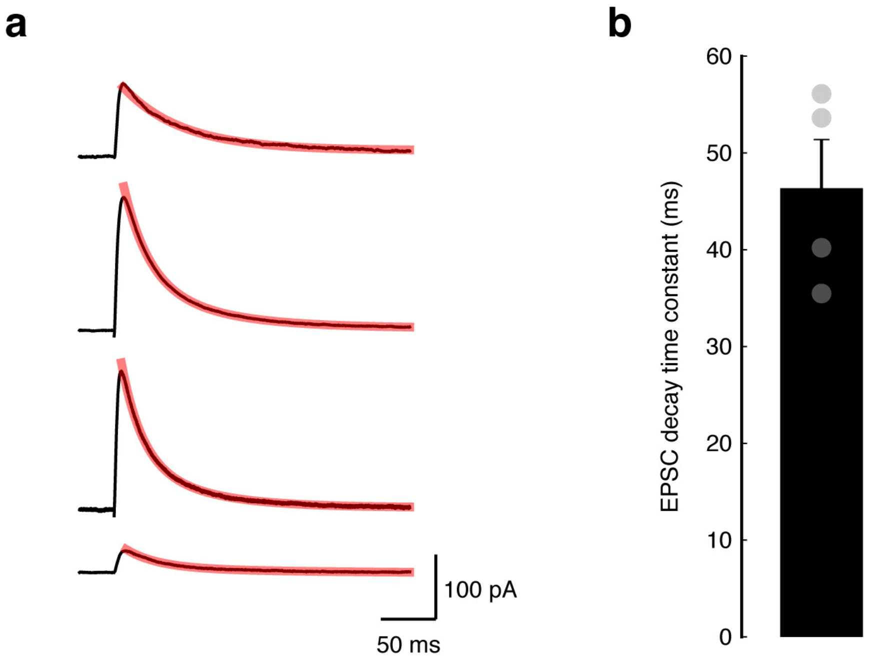

**Supplementary Figure 17**

NMDAR-mediated EPSC kinetics in MECII stellate cells.

(**a**) Somatic voltage clamp recordings from MECII stellate cells. EPSCs were evoked by extracellular stimulation in layer I of MEC. Currents were recorded at a holding potential of +40 mV in the presence of NBQX and SR95531 to isolate NMDAR-mediated EPSCs. Black traces show averages of 50–100 sweeps from 4 different MECII stellate cells. Stimulus artefacts were blanked. Amplitude-weighted decay time constants were determined from biexponential fits to the decay phase of the EPSCs (red).

(**b**) Summary of NMDAR-mediated EPSC decay time constants in MECII stellate cells (mean 46 ± 5 ms; *n* = 4 cells).

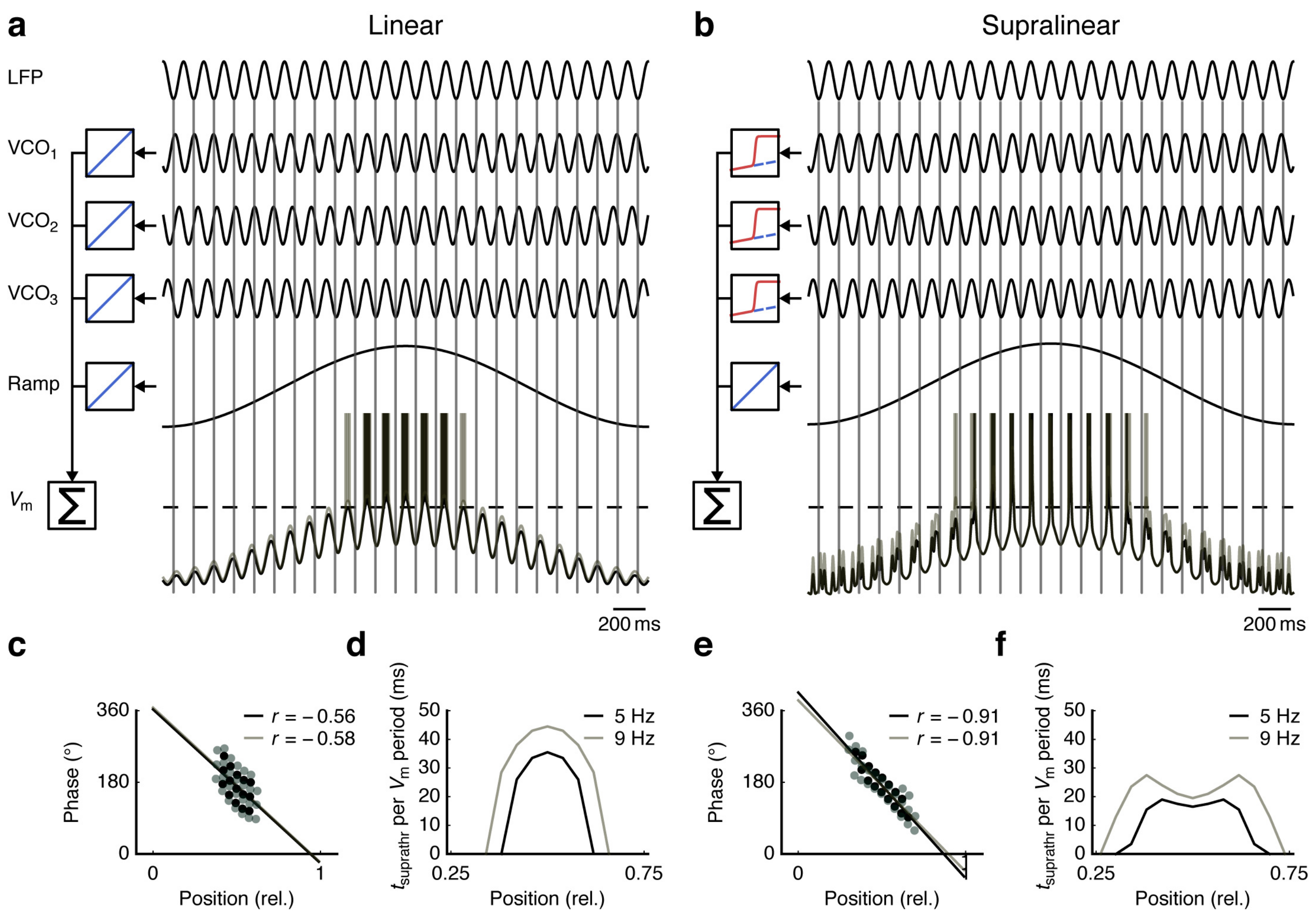

**Supplementary Figure 18**

Fast supralinear integration can sharpen phase precession.

(**a**,**b**) In a basic implementation of an oscillatory interference model, 3 velocity-controlled oscillators (VCO) are summed up either linearly (**a**) or supralinearly (**b**), resulting in an oscillatory interference pattern of membrane potential (bottom traces). Spikes occur whenever the compound oscillation crosses spike threshold (dashed lines).

(**c**,**e**) The phase of spikes with respect to the local field potential (LFP) is plotted against relative position in the firing field. Spikes show phase precession with respect to the LFP. Compared to linear integration (**c**), supralinear integration (**e**) leads to sharpened phase precession within a narrow band around the fitted line.

(**d**,**f**) For each $V_\mathrm{m}$ oscillation period, the time during which $V_\mathrm{m}$ is larger than spike threshold ($t_\mathrm{suprathr}$) is plotted against relative position of the $V_\mathrm{m}$ oscillation peak in the firing field. At the same mean firing rate, linear integration (**d**) leads to larger $t_\mathrm{suprathr}$ in the center of the firing field compared to supralinear integration (**f**), where $t_\mathrm{suprathr}$ in the center is lower and more distributed across the firing field. As a consequence, supralinear integration restricts spiking to a smaller time window during each $V_\mathrm{m}$ oscillation period, leading to sharper phase precession. Grey traces were obtained by increasing the slope of the linear function (**a**, **c**, **d**) or the amplitude of the supralinear function (**b**, **e**, **f**) to yield a mean firing rate of 9 Hz.

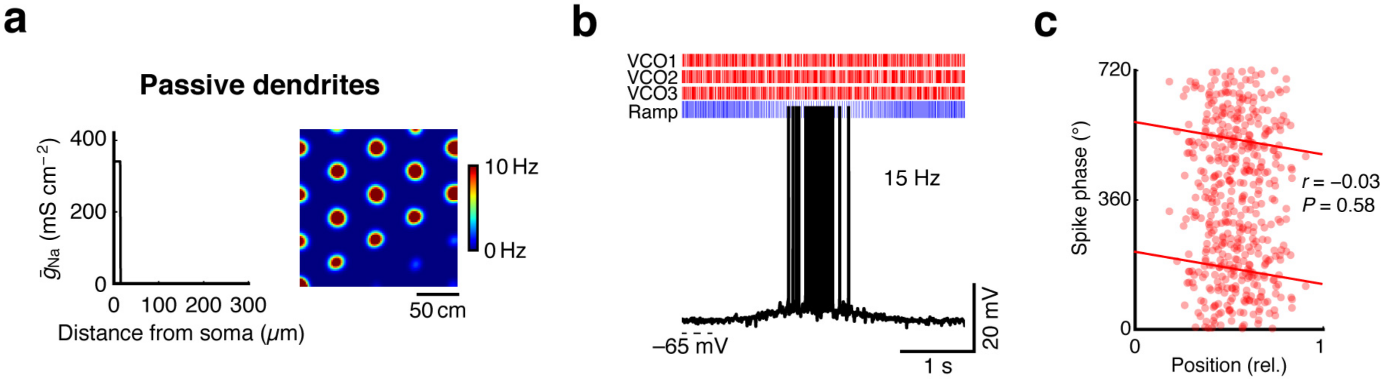

**Supplementary Figure 19**

Degraded phase precession in a compartmental model with passive dendrites.

(**a**–**c**) Same plots as in Fig. 6a–c for a model with passive dendrites. In the simulations shown here, amplitudes of excitatory synaptic conductance changes were increased to yield the same spatial width of grid fields as in the active model (Fig. 6d–f). Phase precession further degraded compared to the model with weaker synaptic inputs (Fig. 6c). Red lines represent a circular-linear regression (*n* = 239 spikes).

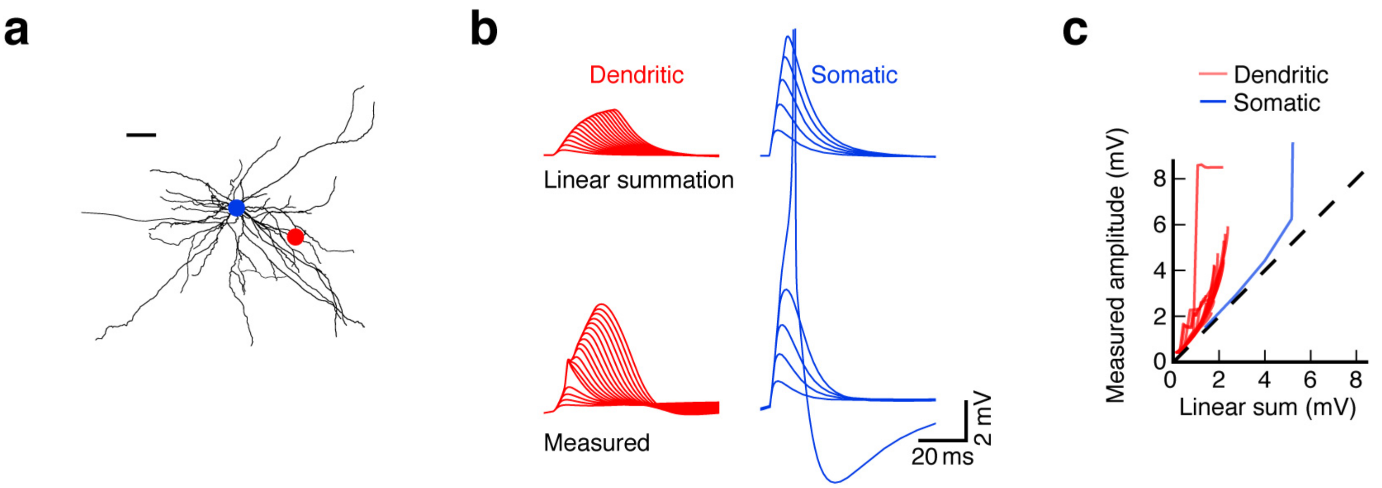

**Supplementary Figure 20**

NMDARs must be dendritic to make integration supralinear.

(**a**) Model neuron based on a published morphology (Garden *et al*., 2008) with the location of a dendritic (red) and a somatic (blue) synaptic conductance change indicated.

(**b**) Top traces show the arithmetic sum of model responses to stimulation of individual synapses on a single dendritic branch (red) or at the soma (blue). Bottom traces show the model responses to activating an increasing number of synapses at an interval of 1 ms.

(**c**) Input-output curves of individual dendritic branches of the same model cell (red) and of a somatically located synapse (blue)

A somatically located synapse will produce somatic action potentials before NMDARs can be recruited. In contrast, a dendritic synapse can recruit NMDARs as the local EPSP amplitude at the synaptic site is sufficiently large to relieve $Mg^{2+}$ block, and the EPSP is substantially attenuated while it propagates to the soma.